ELSEVIER

Contents lists available at ScienceDirect

# Mechanics of Materials

journal homepage: www.elsevier.com/locate/mechmat





# Multiresolution investigations of thermally aged steels using spherical indentation stress-strain protocols and image analysis

Almambet Iskakov <sup>a</sup>, Surya R. Kalidindi <sup>a,b,\*</sup>

- <sup>a</sup> George W. Woodruff School of Mechanical Engineering, Georgia Institute of Technology, Atlanta, GA, 30332, USA
- <sup>b</sup> School of Computational Science and Engineering, Georgia Institute of Technology, Atlanta, GA, 30332, USA

#### ARTICLE INFO

Keywords:
Multiresolution
Mechanical evaluation
Spherical indentation
Image analysis
High throughput
Thermally aged steels

#### ABSTRACT

In recent work, our research group has developed and demonstrated novel multi-resolution protocols capable of extracting indentation stress-strain (ISS) curves from tests on individual microscale constituents (e.g., phases, grains) as well as bulk properties of material microstructures. In addition, we recently developed protocols for design of consistent segmentation of micrographs. This work combines these recent advances in multi-resolution spherical indentation and image segmentation protocols to address the current challenges in the critical evaluation and advancement of physics-based composite models. These new research avenues are identified and demonstrated through a case study on thermally aged ferrite-pearlite steel samples, where the respective indentation yield strengths of the microscale constituents (i.e., ferrite, and pearlite) and the bulk yield strength of the samples were estimated from ISS tests measurements. The constituent volume fractions were extracted from segmented optical microscopy images. It is shown that the multi-resolution indentation yield strength and volume fraction measurements are highly consistent with the homogenization estimates from simple composite theories.

#### 1. Introduction

The individual properties of the microscale constituents (i.e., distinct thermodynamic phases) and their complex spatial arrangements in the material's representative volume (i.e., microstructure) control the effective mechanical properties of metal alloys (Tasan et al., 2015; Lütjering, 1998; Murayama and Hanada, 2002; Bian et al., 2015; Joost, 2012; Javidani and Larouche, 2014). For example, steel alloys are often comprised of hard constituents (e.g., pearlite, martensite) in a soft ferrite matrix. The microstructural details of these alloys are known to influence strongly their effective properties (e.g., strength, ductility (Tasan et al., 2015; Syn et al., 1994; Schemmann et al., 2015; Hüseyin et al., 2010; Pan et al., 2018)). The physics connecting the properties of the microscale constituents to the effective properties of the material has been the focus of many prior studies (Gerbig et al., 2018; Allison et al., 2006; Wu et al., 2015; Zhu et al., 2019). Indeed, physics-based composite theories (i.e., homogenization models) have offered avenues to study the complex relationships between the constituent properties, the microstructural details, and the effective properties of the material (Allison et al., 2006; Hill, 1952; Eshelby, 1957; Kröner, 1977; Mori and Tanaka, 1973; Torquato, 2002; LLorca et al., 2011; González et al., 2017; Segurado et al., 2003; Suquet, 1985; Nemat-Nasser and Hori, 2013; Segurado and Llorca, 2013; Matouš et al., 2017). However, in practice, one often does not have adequate information on the constituents' properties or the microstructural details or both.

Indeed, studies of the scaling relationships for the mechanical properties of a heterogeneous material at multiple length scales have encountered formidable challenges. The first major challenge comes from the need to measure the mechanical properties of individual microscale constituents at very small length scales that must be performed on very small material volumes, often on the order of microns (Ghassemi-Armaki et al., 2014; Kumar et al., 2006, 2014). Most of the current microscale mechanical characterization methods (e.g., miniaturized tension tests, micropillar compression) incur substantial cost and effort, and produce very limited data (i.e., low throughput). However, mechanical evaluation at the macroscale is usually performed using standardized protocols such as uniaxial tension (ASTM, 2003) and compression (ASTM, 2000) tests. One often finds significant differences in the measured mechanical properties at the microscale and the macroscale, and often reconciles them as consequences of material length scale effects (Tabor, 2000; Hill et al., 1947; Johnson, 1970; Pharr et al., 2010; Nix and Gao, 1998; Qian et al., 2005; Rodriguez and

<sup>\*</sup> Corresponding author. George W. Woodruff School of Mechanical Engineering, Georgia Institute of Technology, Atlanta, GA, 30332, USA. E-mail address: surya.kalidindi@me.gatech.edu (S.R. Kalidindi).

Gutierrez, 2003; Swadener et al., 2002; Zhang et al., 2011). It is entirely possible that the vast differences in the measurement protocols used at the different length scales are contributing significantly to the reported differences in the measurements obtained at the different length scales. The inability to reconcile fully the differences in the measured mechanical properties at the different material/sample length scales had hindered our ability to advance a reliable and consistent homogenization modeling framework for metal alloys.

There have been several efforts to evaluate constituents' properties at the lower length scales using miniaturized versions of the same uniaxial tension (Kumar et al., 2006, 2014) and compression (Ghassemi-Armaki et al., 2014; Bei et al., 2008) tests employed in the macroscale evaluations. However, these efforts have faced significant hurdles due to the challenges involved in the fabrication of samples and the highly specialized test setups. As a significantly lower-cost and a higher-throughput alternative, indentation techniques offer a much different research avenue for the multiresolution mechanical evaluation of heterogeneous materials (Rodriguez and Gutierrez, 2003; Tabor, 1948; Walley, 2012; Fischer-Cripps, 2006; Oliver and Pharr, 1992, 2004; Brinell, 1900). Traditionally, indentation was performed with sharp tip geometries (e.g., Berkovich, Vickers) (Oliver and Pharr, 1992). However, the conventional protocols only estimated hardness values at a specified load/depth and were not easily transformed to intrinsic material properties that can be related to those measured in the standard tension/compression tests (Rodriguez and Gutierrez, 2003; Zhang et al., 2011; Tabor, 1948; O'Neill, 1967; Tirupataiah and Sundararajan, 1991). Prior studies have generally reported high variability in the indentation measurements on the same material and across different length scales (Pharr et al., 2010; Nix and Gao, 1998; Rodriguez and Gutierrez, 2003; Swadener et al., 2002), making it difficult to use these measurements to critically evaluate the existing homogenization models. In recent work (Pathak and Kalidindi, 2015; Vachhani et al., 2016; Weaver et al., 2016a; Gong et al., 2017; Khosravani et al., 2018, 2020; Parvinian et al., 2020; Millan Espitia et al., 2020), our research group has developed and demonstrated novel protocols capable of extracting indentation stress-strain (ISS) curves using spherical indenter tips (Pathak and Kalidindi, 2015; Kalidindi and Pathak, 2008; Pathak et al., 2009a). The consistency and fidelity of these protocols have been demonstrated at multiple material length scales (Vachhani et al., 2016; Weaver et al., 2016a, 2016b, 2017; Khosravani et al., 2020, 2021; Pathak et al., 2008, 2009a, 2009b, 2012, 2016; Vachhani and Kalidindi, 2015; Weaver and Kalidindi, 2016) using different indenter tip radii. These demonstrations have included measurements within regions inside individual grains (Weaver et al., 2016a; Pathak et al., 2008, 2009b, 2016; Vachhani and Kalidindi, 2015; Weaver and Kalidindi, 2016) as well as on an ensemble of grains (Khosravani et al., 2017, 2018, 2020; Weaver et al., 2016b; Iskakov et al., 2018; Bhat and Neu, 2020). The protocols have been validated both against the measurements on samples where ground-truth data (from standard tension tests) was available (Khosravani et al., 2020; Weaver et al., 2016b; Iskakov et al., 2018; Bhat and Neu, 2020) as well as the numerical simulations of the indentation experiment (Donohue et al., 2012; Patel and Kalidindi, 2016). Since these protocols employ a consistent framework for measurements at both the constituents' scale and the macroscale, they offer a new avenue for the critical evaluation and the refinement of homogenization models.

The second major challenge in the study of the homogenization models for heterogenous materials comes from the need to obtain reliable estimates of the relevant microstructural statistics (e.g., phase volume fractions). Often, the raw microscopy images capturing the microstructural details are produced in grayscale, where each pixel (or voxel) is assigned a grayscale value between 0 and 255. However, the number of distinct microscale constituents (i.e., thermodynamic phases) present in the sample is typically far smaller than the number of grayscales in the raw images. This is because the pixel values of raw images reflect various types of noise arising from a combination of equipment and/or sample conditions. Therefore, segmentation protocols need to be

designed and employed to de-noise the raw microscopy images (i.e., correct the labelling of all pixels/voxels in the image based on the actual constituents present in them) and extract the needed microstructure statistics. Segmentation is generally performed by assembling a workflow comprising a sequence of image processing functions and filters (Smith et al., 2018; Santofimia et al., 2008; Paredes-Orta et al., 2019; Payton et al., 2010; Campbell et al., 2018). Often, the successful construction and implementation of the workflow leading to accurate segmentation is highly dependent on the user's expertise in the application of the image processing functions. Consequently, such efforts often lead to non-standard approaches that can strongly influence the accuracy of the microstructure analysis. Very recently, we have developed and demonstrated a systematic framework for designing segmentation workflows that reduces the dependence on the user's expertise (Iskakov and Kalidindi, 2020); these segmentation workflows utilize image processing functions from popular software packages such as Python (Perez et al., 2011) and MATLAB (Higham and Higham, 2016), enabling potentially broad adoption by the material science community.

The recent advances in multi-resolution spherical indentation and image segmentation described above have now set the stage for systematic investigations of the mechanical responses of metal alloys and the critical evaluation of available composite theories. In this work, we conduct such an investigation into the mechanical response of thermally aged ferrite-pearlite steel samples. These samples were selected because they represent typical thermal aging conditions encountered in industrial power generation applications (e.g., high-temperature piping, gas turbine housing) (Bierdel et al., 2013; Pérez et al., 2011; Kruger et al., 2017). The prolonged thermal exposures (thousands of hours) in these samples contributed to significant changes in the microstructures as well as their yield strengths (Pérez et al., 2011; Kruger et al., 2017; Foulds and Shingledecker, 2015; Foulds and Viswanathan, 2001; Pantazopoulos et al., 2016). In this work, we have employed the spherical indentation protocols on both the individual microscale constituents (i. e., ferrite, pearlite) and at the macroscale. The respective indentation yield strengths of the microscale constituents and the bulk yield strength of the sample were estimated from these measurements. The constituent volume fractions in these samples were extracted from segmented optical microscopy (OM) images. All of this information was used to evaluate the composite theory estimates based on some of the simple homogenization models used in current literature (Cho and Gurland, 1988; Giannakopoulos et al., 1995; Williamson et al., 1993; Stringfellow and Parks, 1991; Latypov and Kalidindi, 2017). It is shown that the multiresolution spherical indentation and image segmentation protocols employed in this work produce results that are highly consistent with the homogenization estimates for these material systems from the simple composite theories. The novel high-throughput multi-resolution mechanical characterization protocols presented in work offer a powerful new toolset for the critical study of homogenization models for heterogeneous material systems.

# 2. Materials and methods

# 2.1. Thermally aged steel samples

In this work, multiresolution mechanical evaluation is performed on three 0.3% C steel samples with the different levels of thermal exposure that represent typical thermal aging conditions experienced in industrial power generation applications. The three samples in this work are labelled based on the levels of thermal aging exposure in typical applications as 'unexposed' (i.e., no thermal exposure), 'moderate exposure', and 'high exposure'. It is important to reiterate that the initial alloy material was the same for all samples. The ferrite-pearlite steels exhibit a microstructure that initially consists of two constituents, ferrite and pearlite, as shown in Fig. 1a. The ferrite is made up of  $\alpha$ -ferrite, and the pearlite is comprised of lamellar arrangement of  $\alpha$ -ferrite and cementite (Fe<sub>3</sub>C) phases. The  $\alpha$ -ferrite phase consists mainly of iron with small

**Fig. 1.** Example optical microscopy (OM) images at different magnifications for different levels of thermal exposure. a) unexposed sample with ferrite (f) and lamellar pearlite (p), b) moderate exposure sample with pearlite spheroidization, and c) high exposure sample with pearlite spheroidization and graphitization (g).

amounts of interstitial carbon, and is the softer microscale constituent in the samples. The lamellar pearlite serves as the harder microstructure constituent because of the hard cementite phases. Thermal exposure of these steels generally leads to significant changes in the microstructure and the bulk mechanical properties (Syn et al., 1994; Kruger et al., 2017; Pantazopoulos et al., 2016; Okamoto, 1989). At moderate levels of thermal exposure, the lamellar pearlite undergoes spheroidization (Foulds and Viswanathan, 2001; Pantazopoulos et al., 2016; Marder and Bramfitt, 1976). An example of this transformation can be seen in the optical micrograph in Fig. 1b. At higher levels of exposure, in addition to spheroidization, one also observes graphitization, as seen in the optical micrograph in Fig. 1c. Graphitization results from the diffusion of carbon from  $\alpha$ -ferrite and cementite phases to form secondary graphite particles (Pérez et al., 2011; Kruger et al., 2017; Foulds and Shingledecker, 2015; Foulds and Viswanathan, 2001; Pantazopoulos et al., 2016). In this study, both spheroidization and graphitization are observed in the thermally exposed samples.

#### 2.2. Sample preparation

Samples studied in this work were mounted in standard epoxy resin such that the sample surface is exposed on both opposing sides. The samples were ground on both sides to ensure parallel surfaces needed for the indentation tests. For microindentation and optical microscopy, the sample surfaces were polished up to 0.02 µm colloidal alumina suspension and vibropolished in a 4:1 ratio of water to colloidal silica mixture as the final step, which resulted in the slightly etched surfaces shown in Fig. 1. The slight etching of the sample surface enabled clear identification of lamellar and spheroidized pearlite grains, as well as the graphite particles. For nanoindentation, the samples were further electropolished, in an electrolyte consisting of 6% perchloric acid (60%), 14% distilled water, and 80% ethanol (ASTM, 2009), to minimize any remaining scratches from mechanical polishing. The electropolishing process clearly revealed the phase boundaries between the ferrite and pearlite constituents, and allowed the selection of nanoindentation sites away from the phase boundaries.

#### 2.3. Image segmentation

For the microstructures of the steel samples shown in Fig. 1, the three microstructural constituents of interest are ferrite, pearlite, and graphite. Segmentation of the microscopy images obtained in this work was performed following our recently developed framework for segmentation workflows (Iskakov and Kalidindi, 2020). This framework utilizes a sequence of five steps. The first step addresses best practices in experimental image acquisition including sample preparation, selection, and setup of image acquisition equipment and parameters. The second

step addresses preprocessing of raw images (e.g., noise reduction, adjustment, and enhancement) to prepare them for segmentation. The third step applies various segmentation algorithms to label each image pixel with the expected local state. The fourth step deals with post-processing of the segmented images. The final step focuses on the evaluation and validation of the segmentation results.

In the present study, images were captured using a Zeiss Observer A1.m light optical microscope. To strike a balance between capturing sufficient details of pearlite spheroidization and a representative distribution of ferrite-pearlite grains in each image, a view field of 312  $\times$  312  $\mu m$  was chosen, which corresponds to a spatial resolution of 0.3  $\mu m/$  pixel in 1040  $\times$  1040 pixel images. A magnified portion of a typical acquired image for high exposure sample is shown in Fig. 2a. Microscope image acquisition parameters were adjusted to provide as much contrast as possible for spheroidized pearlite grains.

The next step in the segmentation workflow addressed image noise reduction and contrast enhancement of the features of interest. Image noise reduction was tackled both on the image-scale (i.e., reducing unwanted intensity gradient over the image) and pixel-scale (i.e., reducing random variation of individual pixel intensities). The image-scale gradient was reduced by subtracting an approximated shadow profile from the noisy image (Iskakov and Kalidindi, 2020). Random pixel-scale noise throughput the image was removed using Gaussian filtering (Soille, 2013). It is important to note that optimal filtering of random noise requires a balance between noise reduction and retention of feature details (e.g., details of feature edges). In this study, an optimal Gaussian filtering strength was chosen based on the lowest similarity between the removed random noise and the filtered image (Iskakov and Kalidindi, 2020). Following noise reduction, contrast enhancement was performed on the whole image using contrast stretching (Gonzalez and Woods, 2002), which increases the difference in intensity values throughout the image.

Next, the segmentation step is performed to label each image pixel with one of the three local states of interest identified earlier - ferrite, pearlite (lamellar or spheroidized) or graphite. An intensity thresholding approach was utilized, which separates the image intensities into k+1 classes using k thresholds. In the present work, the pixels in each image are separated into three classes using the multi-Otsu threshold approach (Otsu, 1979). The resulting segmentation labelled the image pixels into the desired three classes. An example outcome from this procedure is shown in Fig. 2b for the raw image shown in Fig. 2a. In Fig. 2b, the three different microstructural local states are colored differently for the high exposure sample, where the pearlite appears as clusters of spheroidized cementite. Additional clean-up tasks are performed in the post-processing step.

The main goal of the post-processing step is to reassign incorrectly labelled pixel values using intensity thresholding segmentation to their

Fig. 2. Illustration of the individual steps in the segmentation workflow developed and implemented on the images studied in this work. The images shown are for a sample with high exposure. a) Acquired raw image from optical microscopy, b) segmented image showing three microstructural states, and c) post-processed image.

correct microstructural feature labels or filter out unwanted objects from further analysis. For current segmented images, image closing (Soille, 2013) was first performed to connect the clustered pearlite particles seen in Fig. 2b. Image closing is a sequence of dilation (expansion of object boundaries) and erosion (shrinking of object boundaries). The resulting connected clusters represent the regions of the pearlite constituents (lamellar or spheroidized) in the micrographs. Next, several types of incorrectly labelled features were cleaned up in the ferrite matrix. First, small round features with lower intensities (i.e., darker in grayscale) that were labelled as graphite were relabeled as part of ferrite matrix because they likely correspond to material inclusions and/or pitting during the polishing process. Then, pixels directly surrounding graphite particles were reassigned to ferrite if they were incorrectly labelled as pearlite. This incorrect labelling was observed in ferrite matrix that surrounded graphite particles, where the ferrite was noticeably darker (lower intensity) and was incorrectly labelled as pearlite. Finally, single pixel-scale particles that belonged to other microstructure states throughout the ferrite matrix were relabeled to ferrite. This likely resulted from the few highly noisy pixels that remained after the preprocessing step. As mentioned earlier, noise reduction requires a balance between elimination of noise and retention of detail, which typically leaves few noisy pixels that are then labelled incorrectly during the segmentation step. An example of the final post-processed image for the high exposure sample is shown in Fig. 2c.

The final step of the segmentation workflow focuses on the validation of the post-processed segmentation results to assess the confidence in the segmentation results. In practice, segmentation validation can be a challenging process because the ground truth for most studied microstructures is not available. Studies involving materials images often rely on qualitative visual inspection (Payton et al., 2010; Peregrina-Barreto et al., 2013; Collins et al., 2009) due to ease of validation or unavailability of other means. In this work, the validation was performed visually by overlaying the outlines of segmented features over the original grayscale images to check the accuracy with which the different constituent boundaries are captured. For the present work, visual inspection provided reasonable validation since the constituents were clearly distinguished from each other in the micrographs.

# 2.4. Multiresolution mechanical testing using spherical indentation protocols

Indentation analysis protocols are largely based on Hertz theory (Hertz et al., 1896), which describes a frictionless contact between two elastic bodies with quadratic surfaces by the following equations:

$$P = \frac{4}{3} E_{eff} R_{eff}^{V_2} h_e^{3\gamma}, \tag{1}$$

$$\frac{1}{E_{eff}} = \frac{1 - \nu_i^2}{E_i} + \frac{1 - \nu_s^2}{E_s},\tag{2}$$

$$\frac{1}{R_{eff}} = \frac{1}{R_i} + \frac{1}{R_s},\tag{3}$$

where P and  $h_e$  denote indentation load and elastic indentation displacement, respectively, E and  $\nu$  are the Young's modulus and Poisson ratio, respectively, and R denotes the radius. Subscripts s and i correspond to the sample and indenter, respectively, while  $E_{eff}$  and  $R_{eff}$  denote the effective elastic modulus and the effective radius of the indenter-sample system, respectively.

The central strategy in the spherical indentation stress-strain protocols employed in this work is to utilize Hertz's theory to estimate  $E_{eff}$ from the initial elastic loading segment (before the onset of any plastic deformation in the sample), and subsequently use the same value of  $E_{eff}$ to estimate the evolving  $R_{eff}$  by analyzing the elastic unloading segments (again using Hertz's theory). Although Hertz's theory is broadly applicable at the different lengths of interest in this study, the use of different indenter tip sizes requires the use of different equipment and somewhat different protocols. The indentations evaluating the bulk properties of the sample were performed using a large spherical indenter tip (6.35 mm radius in this work), and are referred as microindentation stress-strain protocols. On the other hand, the indentations performed in the microscale constituents using the much smaller indenter tips (16-100 μm radii) were performed in an instrumented nanoindenter equipped with continuous stiffness measurement (CSM) (Vachhani et al., 2016; Weaver et al., 2016a, 2017; Khosravani et al., 2020; Pathak et al., 2008, 2009b, 2012, 2016; Vachhani and Kalidindi, 2015; Weaver and Kalidindi, 2016). It should be noted that the size of the primary deformation zone under the indenter in our protocols roughly corresponds to one-tenth of the indenter tip radius. Therefore, the two sets of measurements described above with the microindenter and the nanoindenter are ideal for the estimation of the bulk properties of the sample and the local properties of the constituents, respectively.

Microindentations were performed using a ZwickRoell Z2.5 hardness tester with a 6.35 mm radius spherical indenter tip ( $R_i$ ) using multiple load-unload cycles (see Fig. 4a). At every cycle, the unload segment is utilized to estimate the contact radius at the peak load for that cycle, and consequently produces one data point on the microindentation stress-strain curve shown in Fig. 4b (Pathak et al., 2009a). The first step of the analyses is focused only on the initial fully elastic load cycle (shown as magenta colored points in Fig. 4a). This first analyses step has two goals: (i) estimate the initial contact between the indenter and the sample (i.e., zero-point correction (Kalidindi and Pathak, 2008)), and (ii) estimate the elastic modulus of the indenter-sample system,  $E_{eff}$ . Zero-point correction is critical to mitigate commonly encountered

contact issues related to both the sample (e.g., surface roughness, surface oxide layer) and the indenter (e.g., shape imperfections). The estimation of zero-point load and displacement correction ( $P^*$  and  $h^*$ ) for indentation without CSM signal has been outlined in prior work (Pathak et al., 2009a) and is performed using a recast version of Eq. (1):

$$(\widetilde{h}_e - h^*) = k(\widetilde{P} - P^*)^{\frac{2}{3}}, \quad k = \left[\frac{3}{4} \frac{1}{E_{eff}} \frac{1}{\sqrt{R_{eff}}}\right]^{2/3},$$
 (4)

 $\widetilde{P}$  and  $\widetilde{h}$  are the raw load and displacement measurements, respectively. During the initial elastic loading on a flat sample surface, shown in Fig. 3a, the effective radius of the indenter-sample system is equal to the radius of the indenter, i.e.,  $R_{eff} = R_i$ . The values of  $h^*$  and  $E_{eff}$  are estimated by performing regression on  $\widetilde{h}_e$  (for the initial fully elastic segment this is equal to the total indentation depth) and  $\widetilde{P}$  in Eq. (4), whereas the value of  $P^*$  is selected as one that minimizes the log of the average absolute error of the regression fit. In microindentation experiments, the sample surface and tip disparities are very small compared to the tip radii, and in many cases,  $P^*$  can be set to zero.

After the initiation of plastic deformation in the sample (see Fig. 3b and c), the total displacement,  $h_t$ , is assumed to comprise of the elastic displacement estimated by Hertz's theory and a residual displacement,  $h_r$ :

$$h_t = kP^{2/3} + h_r. {5}$$

The coefficients k and  $h_r$  are determined using regression techniques on the measured load and total displacement during the unloading segments shown in Fig. 4a (the segment corresponding to 95-50% of the peak force from each unloading segment is used in the analyses performed in this study).  $R_{eff}$  evolves continuously with plastic deformation under the indenter and its value is extracted using Eq. (4) on each unloading segment, where  $E_{eff}$  is assumed to remain constant (established from the initial elastic segment). This is a reasonable assumption because the average plastic deformations are very small in the indentation tests. The evolution of  $R_{eff}$  with increasing indentation depth follows similar trends as those reported in prior work (Pathak et al., 2009a). The contact radius, a, is then determined using the relation derived from Hertz theory:

$$a = \sqrt{R_{eff}(h_t - h_r)}. (6)$$

The indentation stress,  $\sigma_{ind}$ , and the indentation strain,  $\varepsilon_{ind}$ , corresponding to the peak loading point in each unloading segment are defined (Kalidindi and Pathak, 2008) as:

$$\sigma_{ind} = \frac{P_{max}}{\pi a^2}, \varepsilon_{ind} = \frac{4h_t}{3\pi a} \approx \frac{h_t}{2.4a}.$$
 (7)

As mentioned earlier, each unloading cycle produces one point on the microindentation stress-strain curve (see Fig. 4b). Because the indentation stress-strain curve consists of discrete data points, the indentation yield strength is determined using the intersection of a 0.2% strain offset with a linear fit of post elastic data, as shown in Fig. 4b.

Mechanical evaluation of the ferrite and pearlite constituents has been performed using nanoindentation stress-strain protocols. The measurements have been carried out using an Agilent G200 Nanoindenter equipped with CSM (continuous stiffness measurement) capability using a 100  $\mu m$  radius tip. For all tests, indentations were performed within a single phase region belonging to either ferrite or pearlite constituent. An example indentation site for pearlite is shown in Fig. 5c.

The zero-point corrections for the nanoindentations take advantage of the CSM capability. They are determined using the following variant of the Hertz's theory:

$$S = \frac{3P}{2h_e} = \frac{3(\widetilde{P} - P^*)}{2(\widetilde{h} - h^*)},\tag{8}$$

where S is the elastic unloading stiffness measured with CSM. The  $P^*$  and  $h^*$  (i.e., zero-point corrections on indentation load and indentation depth, respectively) are obtained by performing a linear regression on the measurements in the initial elastic loading segment by recasting Eq. (8) as (Kalidindi and Pathak, 2008)

$$\widetilde{P} - \frac{2}{3}S\widetilde{h}_e = -\frac{2}{3}h^*S + P^*. \tag{9}$$

After the zero-point corrections have been applied, the effective elastic modulus,  $E_{eff}$ , is extracted from the initial elastic loading segment by performing regression on P and  $h^{3/2}$  (see Eq. (1)). This is possible because during the initial elastic loading the sample surface remains flat and without permanent deformation and  $R_{eff} = R_i$ . As with the microindentation protocols, the  $E_{eff}$  value is assumed to remain constant throughout the test. The evolving indentation contact radius, a, is computed as (also from Hertz's theory)

$$a = \frac{S}{2E_{eff}}. ag{10}$$

Note that when S is available from CSM capability (e.g., while using a nanoindenter), the calculation of contact radius, a, is greatly simplified as opposed to non-CSM indentation (e.g., while using a microindenter) where a is calculated at the peak load before each unload cycle using Eq. (6). However, both Eq. (6) and Eq. (10) are derived from Hertz theory and are therefore fully consistent with each other. Examples of typical load-displacement and extracted nanoindentation stress-strain curves on a pearlite grain are shown in Fig. 5a and b, respectively. Fig. 5b demonstrates a schematic for determining the 0.2% plastic strain offset indentation yield strength that is used in the ferrite and pearlite nanoindentation measurements.

#### 2.5. Composite mechanical properties

Composite theories are used to predict the bulk (effective)

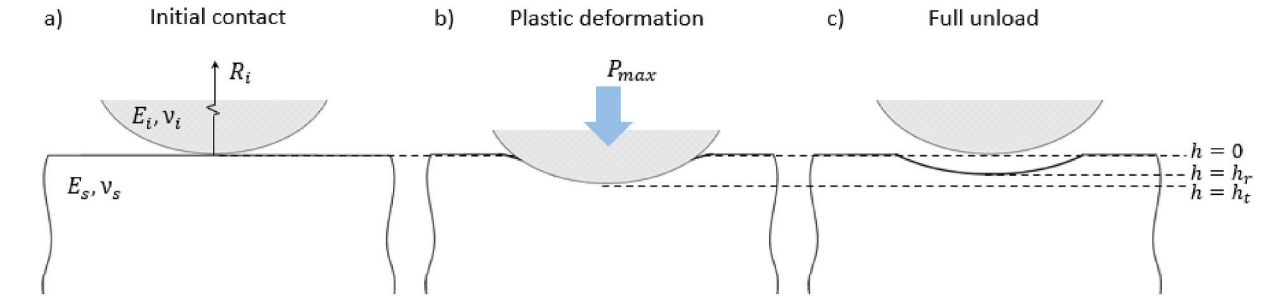


Fig. 3. Schematic of spherical indentation at different stages of the indentation test. a) initial elastic contact between the indenter and the sample, b) load at which plastic deformation has occurred in the sample, and c) complete unload after plastic deformation in the sample.

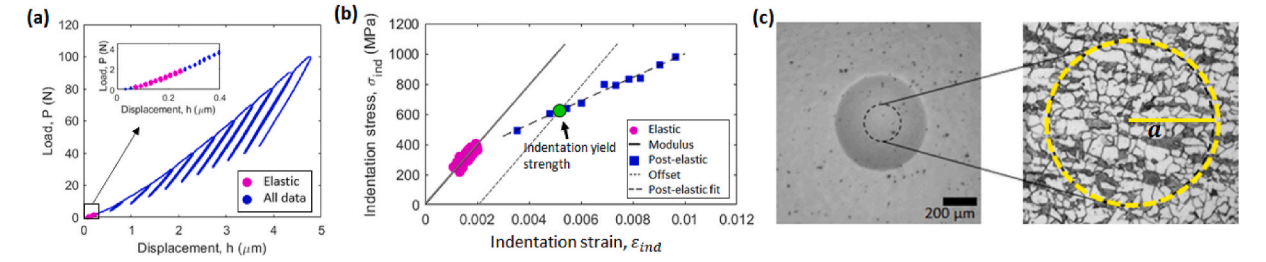
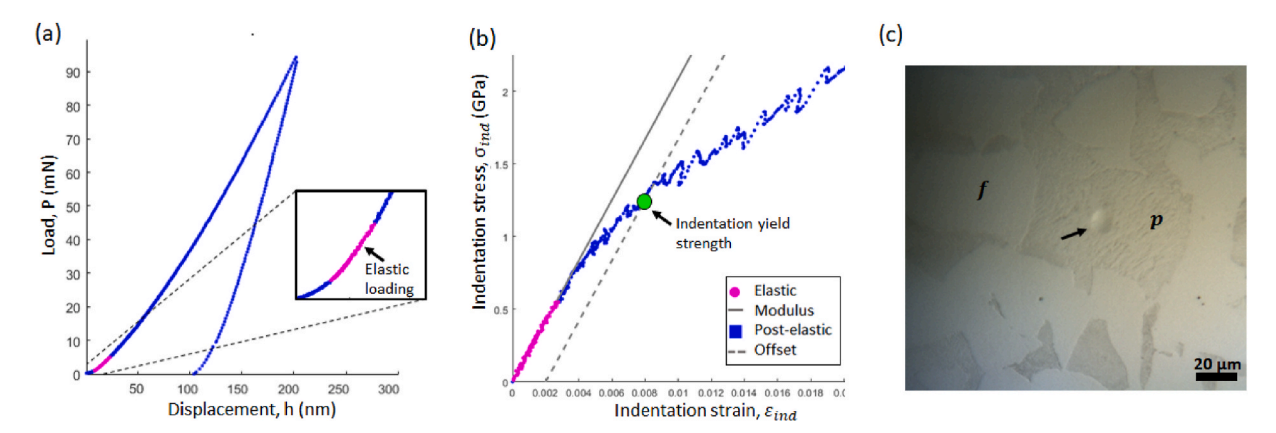


Fig. 4. Example of microindentation stress-strain protocol analysis for unexposed sample. a) typical load-displacement curve with multiple load-unload cycles. The highlighted magenta section corresponds to initial elastic contact used to estimate  $E_{eff}$ . b) Microindentation stress-strain datapoints extracted from the load-displacement data. c) Top view of the residual indentation impression after a test, where the yellow outline corresponds to the contact area at indentation yield stress displayed on an etched sample. (For interpretation of the references to color in this figure legend, the reader is referred to the Web version of this article.)



**Fig. 5.** Example of nanoindentation stress-strain protocol analysis for unexposed sample within a pearlite grain. a) load displacement data with CSM signal. b) Nanoindentation stress-strain curve extracted from the test data. c) Residual indent within a pearlite (*p*) grain (arrow).

mechanical properties as a function of the microstructure statistics and the properties of the microscale constituents. These theories are based on various approaches, including mean-field theories (Molinari et al., 1987; Lebensohn and Tomé, 1993; Tomé, 1999; Nebozhyn et al., 2001), statistical continuum theories (Kröner, 1972, 1977; Brown, 1955; Torquato, 1991, 2013; Torquato and Stell, 1982; Adams and Olson, 1998; Garmestani et al., 1998; Adams et al., 2005, 2012), and computational homogenization (Ghosh et al., 1995; Gilormini and Germain, 1987; Segurado and Llorca, 2002; Geers et al., 2010; Moulinec and Suguet, 1998; Michel et al., 1999; Lebensohn, 2001; Eisenlohr et al., 2013). The simplest of these theories for estimating the effective yield strength of the composite are generally referred as rules of mixtures (Cho and Gurland, 1988; Williamson et al., 1993; Nakamura et al., 2000). These simple estimates are aimed at providing upper and lower bound estimates for the effective yield strength of the composite based on the constituent volume fractions and their respective yield strengths. Other approaches incorporate higher-order microstructure statistics (e.g., statistical continuum theories (Kröner, 1972; Torquato, 1991)) and computational strategies (e.g., finite element models (Segurado et al., 2003; Ghosh et al., 1995; Gilormini and Germain, 1987; Geers et al., 2010; Michel et al., 1999)). Although the more sophisticated approaches can provide higher fidelity estimates, they often also require significantly higher computational effort. A significant hurdle in the advancement of composite theories has been the lack of a sufficiently large experimentally measured dataset of microstructures and their associated properties at both the macroscale and the constituent scale. The availability of such data would be valuable to critically validate and/or refine the different composite modeling approaches. The protocols developed in this work aim to address this gap.

Most composite modelling approaches (including those outlined above) utilize material properties at both the constituent scale and the macroscale that are implicitly defined in a single standardized test mode. By default, the standardized testing mode is selected to be uniaxial test mode (e.g., simple tension, simple compression). However, it is very difficult to conduct the standardized tests at the constituent scale. In the protocols employed in this work, we address this gap by utilizing consistent spherical indentation stress-strain protocols for evaluation of the mechanical properties at both the constituent scale and the macroscale. Consequently, our protocols open new research directions by eliminating any inconsistency in the measurement protocols at the different length scales. For the proper application of the established composite models to the indentation measurements presented in this work, one needs to suitably adapt them. In the simple composite models explored in this work, this adaption is accomplished by introducing suitably Y<sub>i,ind</sub> as the indentation yield strength of the i-th constituent and  $\widetilde{Y}_{ind}$  as the composite indentation yield strength in place of the uniaxial yield strengths typically used in these models. The most convenient way to make this switch is to express the models such that the strength parameters appear as ratios that are independent of the test mode. Specifically, in this work, we assume that  $\frac{Y_{i,ind}}{\widetilde{Y}_{ind}} = \frac{Y_i}{\widetilde{Y}}$ , where  $Y_i$  denotes the uniaxial yield strength of the *i*-th constituent and  $\widetilde{Y}$  is the macroscale uniaxial yield strength of the composite.

A total of three simple composite models were evaluated in this work using the indentation and microstructure quantification protocols presented earlier. The simplest of the models is based on the linear ROM (rule of mixtures) and is adapted here as

$$\widetilde{Y}_{ind} = \sum_{i=1}^{N} V_i Y_{i,ind}, \tag{11}$$

where  $V_i$  is the volume fraction of the i-th constituent (i = 1, 2, ..., N). In the current study, the composite material is treated as a two-phase ferrite-pearlite microstructure because the graphite fraction is rela-

tively low (below 2%) in all samples. The values of the index i=1 and i=2 correspond to the pearlite and ferrite constituents, respectively. The physical parameters for this ROM model are  $V_1$ ,  $V_2$ ,  $Y_{1,ind}$ , and  $Y_{2,ind}$ . Note that in the current study we treat the microstructure as a two-constituent material, therefore  $V_2 = 1 - V_1$ .

The linear ROM shown in Eq. (11) generally provides a higher estimate compared to the composite's yield strength. Consequently, a modified rule of mixtures model has been proposed by Tamura et al. (Tamura and Ozawa, 1973) for an improved estimation of the yield strength of two-phase composites. This approach models the harder phase as elastic and the softer matrix phase as elastic-plastic. This is a reasonable assumption for many multiphase metals, as shown in a study on dual-phase steels (Fischmeister and Karlsson, 1977). For the present work, the composite indentation yield strength from this model can be adapted as

$$\widetilde{Y}_{ind} = Y_{2,ind} \left[ V_2 + \left( \frac{q+E_2}{q+E_1} \right) \frac{E_1}{E_2} V_1 \right],$$
 (12)

where E denotes the elastic modulus, and, as before, i=2 corresponds to the softer ferrite constituent. The parameter, q, is an empirical parameter that exhibits values in the range  $0 \le q \le \infty$ . In a study on dualphase steels, q=4.5 GPa has shown reasonable agreement with experimental results (Fischmeister and Karlsson, 1977); this value was used in this study. In summary, the physical parameters for this modified ROM model are  $V_1$ ,  $V_2$ ,  $E_1$ ,  $E_2$ ,  $Y_{2,ind}$ , and q.

As a more sophisticated modeling option, we have also evaluated a self-consistent model in this study. Specifically, we have used the self-consistent model developed by Stringfellow and Parks (1991). In this approach, the composite is modeled by considering *N* distinct spherical incompressible isotropic inclusions (made of constituent materials) embedded in a homogeneous isotropic effective medium. Elastic deformations are ignored and only the volume fraction information is included in this model. The partitioning ratio of the average equivalent strain rate in each phase to the equivalent strain rate of the composite is expressed as

$$\chi_i = \frac{\dot{\gamma}_i}{\dot{\gamma}^*},\tag{13}$$

where  $\dot{\gamma_i}$  and  $\dot{\gamma}^*$  are the equivalent plastic shear strain rate in the *i*-th phase (constituent) and the composite, respectively. Eq. (13) was intended to be applicable in any deformation mode and is extended here to the indentation deformation modes. A requirement that macroscopic fields are equal to the volume averages of the local fields leads to the self-consistency condition

$$\sum_{i=1}^{N} V_i \chi_i = 1. {14}$$

Stringfellow and Parks (1991) derived the following relations for the partitioning ratios:

$$\chi_i = \frac{5}{3} + \frac{2s_i}{3s^2} \chi_i^{1/m},\tag{15}$$

where  $s_i$  and  $s^*$  correspond to the reference shear strength of each phase and the composite, and m is the strain rate sensitivity. It was also assumed that the ratios of shear strengths can be replaced with the ratios of the yield strengths (i.e., it is assumed that the shear strength and tensile yield strength are related through a single constant). Following our earlier strategy of replacing ratios of the constituent and macroscale yield strength parameters with the corresponding ratios of indentation yield strengths, Eq. (15) is adapted for this work as

$$\chi_{i} = \frac{5}{3} + \frac{2Y_{i,ind}}{3\widetilde{Y}_{i\to i}} \chi_{i}^{1/m}.$$
 (16)

Eq. (16) together with the self-consistency condition in Eq. (14) yield

a closed system of equations that need to be solved for the unknowns  $\chi_i$  and  $\widetilde{Y}_{ind}$ , while using known values of  $Y_{i,ind}$ . Additionally, for the present case, we assign N=2 (i.e., pearlite and ferrite) and m=0.01. In summary, the physical parameters for this self-consistent model are  $V_1$ ,  $V_2$ ,  $Y_{1,ind}$ ,  $Y_{2,ind}$ , and m.

Because there were multiple indentation and volume fraction measurements for each sample, a normal distribution was assumed for all experimental measurements produced in this work. To estimate the distribution of indentation yield strength of each composite model predictions, the input variables were randomly sampled from these distributions. A total of 10,000 samples were extracted and used for each composite model predictions. For each sample, the average and one standard deviation of the composite indentation yield strength predictions,  $\widetilde{Y}_{ind}$ , were reported. The goal is to evaluate the accuracy of the predicted indentation yield strength from the composite models,  $\widetilde{Y}_{ind}$ , to the actual measured macroscale indentation yield strength,  $\widetilde{Y}_{ind}^*$ . We define the mean average percentage error (MAPE) measure between the predicted and the measured indentation yield strengths as

$$MAPE = \left| \frac{\widetilde{Y}_{ind} - \widetilde{Y}_{ind}^*}{\widetilde{Y}_{ind}^*} \right| \times 100.$$
 (17)

#### 3. Results and discussion

### 3.1. Microstructure statistics

For each sample, 10 microstructure images at random sample locations were acquired and segmented. The volume fraction of pearlite,  $V_1$ , was determined for each image as the fraction of the total pixels labelled as pearlite, and as mentioned earlier, the ferrite volume fraction was calculated as  $V_2 = 1 - V_1$ . The average and one standard deviation of the pearlite fractions for each sample are reported in Table 1. For the unexposed sample, the average pearlite volume fraction was 28.9%, whereas for the moderate and high exposure samples, the average pearlite fraction was slightly lower, at 25.7% and 25.0%, respectively. The slight decrease in pearlite fraction for thermally exposed samples is most likely related to the fact that the pearlite constituents are highly spheroidized and the pearlite boundaries are not as clearly defined as in the initial unexposed microstructure.

# 3.2. Spherical microindentation and nanoindentation stress-strain measurements

The results from spherical indentation stress-strain protocols are also summarized in Table 1. The 0.2% offset indentation yield strength at macroscale  $\widetilde{Y}_{ind}^*$  was measured with microindentation, while the corresponding indentation yield strengths of pearlite  $(Y_{1,ind})$  and ferrite  $(Y_{2,ind})$  constituents were measured with nanoindentation. The mechanical tests reveal a trend of decreasing indentation yield strength with increasing thermal exposure, at both the macroscale and microscale. The macroscale properties were evaluated with at least eight microindentation tests in different locations throughout each sample. Given that these indentations involved a large number of grains (see Fig. 4c), it is reasonable to assume that the microindentation measurements represent the bulk material response. This is also evident in the low variation observed in the measured values of the microindentation yield strength,  $\widetilde{Y}_{ind}^*$ , between different locations in the samples, as seen from Table 1.

The microindentation results were compared with the tensile measurements (according to ASTM E8 (ASTM, 2001)) for the unexposed and high exposure samples. Prior work by Patel et al. (Patel and Kalidindi, 2016) has established simple scaling factors for direct comparison of the indentation and uniaxial stress-strain curves, which have demonstrated good agreement in experimental studies (Khosravani et al., 2018;

Table 1
Summary of microstructure statistics and indentation measurements on the thermally aged steel samples. Only the pearlite volume fractions are provided. The balance is assumed to correspond to the ferrite volume fraction.

Sample	Microstructure Information (Segmented OM images)	Nanoindenta	ition measuremen	Microindentation measurements			
	Pearlite %	Pearlite Ferrite		Ferrite		Bulk properties	
	$V_1$	$E_1$ (GPa)	Y <sub>1,ind</sub> (MPa)	E <sub>2</sub> (GPa)	Y <sub>2,ind</sub> (MPa)	E (GPa)	$\widetilde{Y}_{ind}^{*}$ (MPa)
Unexposed	$28.9 \pm 2.1$	$203\pm3.5$	$1047\pm13.4$	$173\pm2.0$	$515 \pm 29.5$	$186 \pm 9.6$	$615\pm18.6$
Moderate exposure	$25.7 \pm 5.7$	$190 \pm 7.0$	$995 \pm 40.2$	$173\pm2.8$	$491\pm25.3$	$187 \pm 9.1$	$544 \pm 14.9$
High exposure	$25.0\pm3.9$	$191\pm3.6$	$715\pm26.2$	$177 \pm 8.2$	$413\pm24.2$	$187 \pm 11.6$	$436\pm32.2$

Iskakov et al., 2018). Patel et al. (Patel and Kalidindi, 2016) also established a scaling factor of 2.0 between the yield strengths extracted using the spherical indentation stress-strain protocols used in this work and the standard uniaxial tests, and was validated experimentally on a broad range of material systems (Weaver et al., 2016b; Khosravani et al., 2021) and steels (Mohan et al., 2021). In this study, we focus on the consistency of the indentation measurements at the two different material length scales. Moreover, to ensure that bulk properties are captured with microindentation, we compare the scaled yield strengths extracted from the microindentation and tensile measurements. The averaged 0.2% plastic strain offset tensile yield strength of unexposed and high exposure samples were 311 MPa and 221 MPa, respectively. The corresponding estimates from the indentation protocols (using the above mentioned scaling factor of 2.0) were 308 MPa and 218 MPa, respectively. These results indicate excellent agreement between

indentation and tensile tests. The tensile modulus of the unexposed and high exposure samples were measured as 205  $\pm$  14.0 GPa and 206  $\pm$  37.5 GPa, respectively. The bulk elastic modulus E, extracted from our microindentation protocols was 186  $\pm$  9.6 GPa for unexposed sample and 187  $\pm$  11.6 GPa for high exposure sample. Most importantly, the trend in the decreasing yield strength with thermal aging is highly consistent between the tension and indentation tests. The results present here provide strong support for our ability to extract reliable estimates of bulk mechanical properties from the microindentation stress-strain protocols described in this work.

The nanoindentation evaluation of ferrite and pearlite grain-scale constituents was performed with a  $100 \, \mu m$  radius indenter tip, so that the primary indentation zone was well within a single grain of ferrite and large enough to include multiple cementite laths or spheroidized cementite particles in pearlite grains (see Fig. 5c). For each sample, at

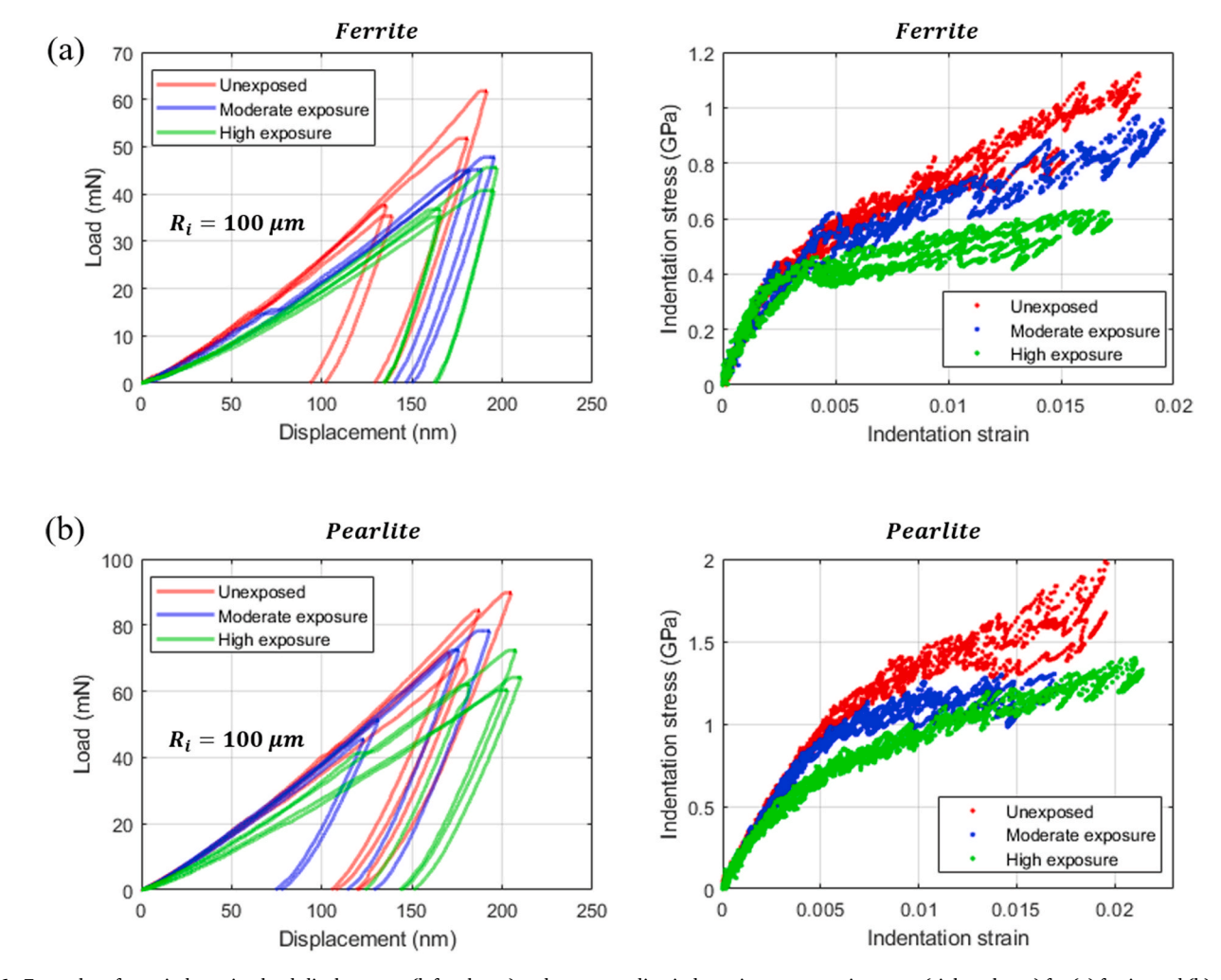


Fig. 6. Examples of nanoindentation load-displacement (left column) and corresponding indentation stress-strain curves (right column) for (a) ferrite and (b) pearlite constituents for all samples.

least eight measurements were made in both ferrite and pearlite constituents. Several examples of load-displacement and corresponding indentation stress-strain curves for nanoindentation measurements are shown in Fig. 6. The elastic modulus and the yield strengths of pearlite and ferrite constituents are also summarized in Table 1. The averaged elastic modulus and the indentation yield strength of ferrite are consistently lower than those of pearlite. Also, the averaged pearlite elastic modulus and indentation yield strength are consistently higher than those obtained from the macroscale measurements with microindentation. This confirms that the bulk modulus and strength of each sample measured in microindentation are indeed bracketed by the respective values for the constituents measured in nanoindentation. It is also seen that the measurements on both ferrite and pearlite constituents reveal a trend of decreasing indentation yield strength with increasing thermal exposure, as seen in Fig. 6. These follow the same trends observed earlier in microindentation.

#### 3.3. Evaluation of composite models

The microstructure information (from segmented micrographs) and the multiresolution indentation measurements were used to critically evaluate the composite models described earlier. These comparisons are summarized in Table 2. The average and one standard deviation of the predicted composite indentation yield strengths,  $\widetilde{Y}_{ind}$ , are presented in this table along with the actual macroscale yield strengths from the microindentation measurements,  $\widetilde{Y}_{ind}^*$ . The linear ROM model produced a consistent overestimation of the composite indentation yield strength, with an average MAPE (mean absolute percentage error) of 11.9% over all three samples. This overestimation is somewhat expected because linear ROM model assumes equal strain in both ferrite and pearlite constituents in estimating the composite properties. On the other hand, the modified ROM consistently underestimated the composite indentation yield strength, with an average MAPE of 11.8%. Note that the estimates using the modified ROM are dependent on the value of the empirical parameter q, which can change significantly form one material to another. The estimates based on Stringfellow-Parks self-consistent model also consistently overestimated the indentation yield strength. However, on average this approach is more accurate than both rule of mixture models, with the average MAPE of 7.5%.

The ROM models represent the simplest of the approaches and experiences the highest deviation from the experimental measurements. As more local microstructure interactions are considered, the selfconsistent model estimates the composite indentation yield strength closer to the actual experimental measurements. The models explored in this work provided both an underestimation and overestimation of the measured bulk yield strength for each sample. It is important to reiterate that these approaches utilize only the ferrite and pearlite constituent volume fractions as microstructure statistics. Yet it is remarkable that even with simple microstructure measures, these models produce reasonable indentation yield strength estimates. Undoubtedly, the use of more sophisticated models that account for other features of the microstructure (e.g., constituents shape and size distributions) are likely to produce more accurate predictions. However, this study is focused on demonstrating the consistency and the reliability of the measurement protocols at the two different material length scales. The results of the simple composite models employed here have provided that confirmation. Nonetheless, the demonstrated protocols can be readily expanded to more sophisticated composite models. For instance, segmented images directly enable quantification of higher-order statistics (e.g., npoint statistics (Torquato and Stell, 1982)) that are necessary in more detailed composite modelling approaches (Torquato, 2013). Moreover, the indentation and image segmentation protocols demonstrated here offer an avenue for aggregation of potentially large datasets for the critical evaluation of various composite theories.

Table 2
Indentation yield strength of pearlite-ferrite steel samples from microindentation measurements and the predicted indentation from three different
composite models. An average MAPE (mean absolute percentage error) for each
model is also provided.

Sample	Microindentation $\widetilde{Y}_{ind}^*$ (MPa)	Linear ROM $\widetilde{Y}_{ind}$ (MPa)	Modified ROM $\widetilde{Y}_{ind}$ (MPa)	Stringfellow-Parks $\widetilde{Y}_{ind}$ (MPa)
Unexposed	<b>615</b> ± 18.6	673 ± 45.5	$516 \pm 29.2$	640 ± 36.7
Moderate exposure	$\textbf{544} \pm \textbf{14.9}$	$620 \pm \\36.2$	$491 \pm 25.5$	$593 \pm 33.9$
High exposure	$\textbf{436} \pm 32.2$	$489 \pm 27.7$	$413 \pm 24.0$	$476\pm23.3$
Average MAPE for each model		11.9%	11.8%	7.5%

#### 4. Conclusions

This work demonstrates the utility and benefits of applying the recently developed protocols for image segmentation and indentation stress-strain measurements for multi-resolution mechanical evaluation of heterogeneous material systems. Specifically, in this work, these protocols were used to study the effects of thermal exposure on the properties of steel samples at both the macroscale and the constituent scale. Image segmentation protocols were used successfully to segment the ferrite and pearlite constituents in the sample microstructures images. Indentation yield strength of the ferrite and pearlite constituents, as well as the bulk indentation yield strength of the samples were evaluated using high-throughput spherical indentation stress-strain protocols. All of the collected microstructure information was used to critically evaluate three composite models used in current literature: rule of mixture, modified rule of mixtures, and a self-consistent model. The predictions from the composite models bracketed the measurements, validating the segmentation and multi-resolution indentation protocols employed in this work. The results of this study offer new avenues for critical evaluation of the multitude composite models being developed and reported in current literature.

#### Credit author statement

**Almambet Iskakov:** Conceptualization, Methodology, Data curation, Formal analysis, Writing – original draft. **Surya R. Kalidindi:** Conceptualization, Funding acquisition, Supervision, Writing – original draft.

# **Declaration of competing interest**

The authors declare that they have no known competing financial interests or personal relationships that could have appeared to influence the work reported in this paper.

#### Acknowledgements

AI and SK acknowledge support from NSF 2027105.

# References

Adams, B.L., Olson, T., 1998. The mesostructure—properties linkage in polycrystals. Prog. Mater. Sci. 43 (1), 1–87.

 Adams, B.L., Gao, X., Kalidindi, S.R., 2005. Finite approximations to the second-order properties closure in single phase polycrystals. Acta Mater. 53 (13), 3563–3577.
 Adams, B.L., Kalidindi, S.R., Fullwood, D.T., 2012. Microstructure Sensitive Design for Performance Optimization. Elsevier Science.

Allison, J., et al., 2006. Virtual aluminum castings: an industrial application of ICME. JOM (J. Occup. Med.) 58 (11), 28–35.

ASTM, E., 2000. E9–89a, standard test methods of compression testing of metallic materials at room temperature. Annu. Book ASTM (Am. Soc. Test. Mater.) Stand. 3, 1–9.

- ASTM, E., 2001. Standard Test Methods for Tension Testing of Metallic Materials. Annual book of ASTM standards. ASTM.
- ASTM, E., 8M, 2003. Standard test methods of tension testing of metallic materials [metric]. In: Annual Book of ASTM Standards.
- ASTM, E., 2009. Standard Guide for Electrolytic Polishing of Metallographic Specimens. Bei, H., et al., 2008. Effects of pre-strain on the compressive stress–strain response of Moalloy single-crystal micropillars. Acta Mater. 56 (17), 4762–4770.
- Bhat, A., Neu, R., 2020. On the constraint factor relating uniaxial and indentation yield strength of polycrystalline materials using spherical microindentation. Mater. Perform. Character. 9 (1), 324–345.
- Bian, J., et al., 2015. Application potential of high performance steels for weight reduction and efficiency increase in commercial vehicles. Adv Manufacture 3 (1), 27–36.
- Bierdel, T., Bullinger, P., Hagedorn, T., 2013. Life Cycle Value for Combined Cycle Power Plants. Siemens AG.
- Brinell, J., 1900. Mémoire sur les épreaves á bille en acier, II. Cong. Int. Methodes d Essai. A. Wahlberg, Paris, p. 243.
- Brown Jr., W.F., 1955. Solid mixture permittivities. J. Chem. Phys. 23 (8), 1514–1517.
   Campbell, A., et al., 2018. New methods for automatic quantification of microstructural features using digital image processing. Mater. Des. 141, 395–406.
- Cho, K., Gurland, J., 1988. The law of mixtures applied to the plastic deformation of twophase alloys of coarse microstructures. Metall. Trans. A 19 (8), 2027–2040.
- Collins, P.C., et al., 2009. Development of methods for the quantification of microstructural features in  $\alpha+\beta$ -processed  $\alpha/\beta$  titanium alloys. Mater. Sci. Eng A. 508 (1–2), 174–182.
- Donohue, B.R., Ambrus, A., Kalidindi, S.R., 2012. Critical evaluation of the indentation data analyses methods for the extraction of isotropic uniaxial mechanical properties using finite element models. Acta Mater. 60 (9), 3943–3952.
- Eisenlohr, P., et al., 2013. A spectral method solution to crystal elasto-viscoplasticity at finite strains. Int. J. Plast. 46, 37–53.
- Eshelby, J.D., 1957. The determination of the elastic field of an ellipsoidal inclusion, and related problems. Proc. Roy. Soc. Lond. Math. Phys. Sci. 241 (1226), 376–396.
- Fischer-Cripps, A.C., 2006. Critical review of analysis and interpretation of nanoindentation test data. Surf. Coating. Technol. 200 (14), 4153–4165.
- Fischmeister, H., Karlsson, B., 1977. Plasticity of two-phase materials with a coarse microstructure. Z METALLKD 68, 311–327.
- Foulds, J.R., Shingledecker, J.P., 2015. An updated assessment of graphitization of steels in elevated temperature service. J. Mater. Eng. Perform. 24 (2), 586–597.
- Foulds, J.R., Viswanathan, R., 2001. Graphitization of steels in elevated-temperature service. J. Mater. Eng. Perform. 10 (4), 484–492.
- Garmestani, H., Lin, S., Adams, B., 1998. Statistical continuum theory for inelastic behavior of a two-phase medium. Int. J. Plast. 14 (8), 719–731.
- Geers, M.G., Kouznetsova, V.G., Brekelmans, W., 2010. Multi-scale computational homogenization: trends and challenges. J. Comput. Appl. Math. 234 (7), 2175–2182.
- Gerbig, D., et al., 2018. Analysis and design of dual-phase steel microstructure for enhanced ductile fracture resistance. Int. J. Fract. 209 (1-2), 3–26.
- Ghassemi-Armaki, H., et al., 2014. Deformation response of ferrite and martensite in a dual-phase steel. Acta Mater. 62, 197–211.
- Ghosh, S., Lee, K., Moorthy, S., 1995. Multiple scale analysis of heterogeneous elastic structures using homogenization theory and Voronoi cell finite element method. Int. J. Solid Struct. 32 (1), 27–62.
- Giannakopoulos, A., et al., 1995. Elastoplastic analysis of thermal cycling: layered materials with compositional gradients. Acta Metall. Mater. 43 (4), 1335–1354.
- Gilormini, P., Germain, Y., 1987. A finite element analysis of the inclusion problem for power law viscous materials. Int. J. Solid Struct. 23 (3), 413–437.
- Gong, X., et al., 2017. High throughput assays for additively manufactured Ti-Ni alloys based on compositional gradients and spherical indentation. Integrating Mater. Manufacturing Innovar. 6 (3), 218–228.
- Gonzalez, R.C., Woods, R.E., 2002. Digital Image Processing, 2 ed. Publishing house of electronics industry, Englewood Cliffs, NJ: Prentice-Hall.
- González, C., et al., 2017. Structural composites for multifunctional applications: current challenges and future trends. Prog. Mater. Sci. 89, 194–251.
- Hertz, H., Jones, D., Schott, G., 1896. Miscellaneous Papers. Macmillan, New York. Higham, D.J., Higham, N.J., 2016. MATLAB Guide, vol. 150. Siam, Philadelphia.
- Hill, R., 1952. The elastic behaviour of a crystalline aggregate. Proc. Phys. Soc. 65 (5), 349.
- Hill, R., Lee, E.H., Tupper, S., 1947. The theory of wedge indentation of ductile materials. Proc. Roy. Soc. Lond. Math. Phys. Sci. 188 (1013), 273–289.
- Hüseyin, A., Havva, K.Z., Ceylan, K., 2010. Effect of intercritical annealing parameters on dual phase behavior of commercial low-alloyed steels. Journal of Iron and Steel Research International 17 (4), 73–78.
- Iskakov, A., Kalidindi, S.R., 2020. A framework for the systematic design of segmentation workflows. In: Integrating Materials and Manufacturing Innovation, pp. 1–19.
- Iskakov, A., et al., 2018. Application of spherical indentation and the materials knowledge system framework to establishing microstructure-yield strength linkages from carbon steel scoops excised from high-temperature exposed components. Acta Mater. 144, 758–767.
- Javidani, M., Larouche, D., 2014. Application of cast Al–Si alloys in internal combustion engine components. Int. Mater. Rev. 59 (3), 132–158.
- Johnson, K., 1970. The correlation of indentation experiments. J. Mech. Phys. Solid. 18 (2), 115–126.
- Joost, W.J., 2012. Reducing vehicle weight and improving US energy efficiency using integrated computational materials engineering. JOM (J. Occup. Med.) 64 (9), 1032–1038.

- Kalidindi, S.R., Pathak, S., 2008. Determination of the effective zero-point and the extraction of spherical nanoindentation stress-strain curves. Acta Mater. 56 (14), 3523–3532.
- Khosravani, A., Cecen, A., Kalidindi, S.R., 2017. Development of high throughput assays for establishing process-structure-property linkages in multiphase polycrystalline metals: application to dual-phase steels. Acta Mater. 123, 55–69.
- Khosravani, A., et al., 2018. Multiresolution mechanical characterization of hierarchical materials: spherical nanoindentation on martensitic Fe-Ni-C steels. Acta Mater. 153, 257–269.
- Khosravani, A., Caliendo, C.M., Kalidindi, S.R., 2020. New insights into the microstructural changes during the processing of dual-phase steels from multiresolution spherical indentation stress-strain protocols. Metals 10 (1), 18.
- Khosravani, A., Thadhani, N., Kalidindi, S.R., 2021. Microstructure quantification and multiresolution mechanical characterization of Ti-based bulk metallic glass-matrix composites. J. Miner. Met. Mater. Soc. 1–11.
- Kröner, E., 1972. Statistical Continuum Mechanics. Springer.
- Kröner, E., 1977. Bounds for effective elastic moduli of disordered materials. J. Mech. Phys. Solid. 25 (2), 137–155.
- Kruger, K., Pistorius, P., Orsmond, C., 2017. Repair welding of carbon steel that has been partially graphitized during service. Weld. World 61 (4), 703–710.
- Kumar, K., Madhusoodanan, K., Rupani, B., 2006. Miniature specimen technique as an NDT tool for estimation of service life of operating pressure equipment. In: International Conference & Exhibition on Pressure Vessel and Piping. Citeseer.
- Kumar, K., et al., 2014. Use of miniature tensile specimen for measurement of mechanical properties. Procedia Eng. 86, 899–909.
- Latypov, M.I., Kalidindi, S.R., 2017. Data-driven reduced order models for effective yield strength and partitioning of strain in multiphase materials. J. Comput. Phys. 346, 242–261.
- Lebensohn, R.A., 2001. N-site modeling of a 3D viscoplastic polycrystal using fast Fourier transform. Acta Mater. 49 (14), 2723–2737.
- Lebensohn, R.A., Tomé, C., 1993. A self-consistent anisotropic approach for the simulation of plastic deformation and texture development of polycrystals: application to zirconium alloys. Acta Metall. Mater. 41 (9), 2611–2624.
- LLorca, J., et al., 2011. Multiscale modeling of composite materials: a roadmap towards virtual testing. Adv. Mater. 23 (44), 5130–5147.
- Lütjering, G., 1998. Influence of processing on microstructure and mechanical properties of  $(\alpha + \beta)$  titanium alloys. Mater. Sci. Eng A. 243 (1–2), 32–45.
- Marder, A., Bramfitt, B., 1976. The effect of morphology on the strength of pearlite. Metall. Trans. A 7 (3), 365–372.
- Matouš, K., et al., 2017. A review of predictive nonlinear theories for multiscale modeling of heterogeneous materials. J. Comput. Phys. 330, 192–220.
- Michel, J.-C., Moulinec, H., Suquet, P., 1999. Effective properties of composite materials with periodic microstructure: a computational approach. Comput. Methods Appl. Mech. Eng. 172 (1–4), 109–143.
- Millan Espitia, N., et al., 2020. Spherical nanoindentation stress-strain curves of primary-  $\alpha$  grains in Ti5-2.5. In: Ti811, Ti64, Ti6242 and Ti6246 Alloys.
- Mohan, S., Pilchak, A.L., Kalidindi, S.R., 2021. Use of Spherical Nanoindentation Protocols to Study the Anisotropic Mechanical Response of Alpha-Beta Single Colonies in Ti-6Al-4V Alloy.
- Molinari, A., Canova, G., Ahzi, S., 1987. A self consistent approach of the large deformation polycrystal viscoplasticity. Acta Metall. 35 (12), 2983–2994.
- Mori, T., Tanaka, K., 1973. Average stress in matrix and average elastic energy of materials with misfitting inclusions. Acta Metall. 21 (5), 571–574.
- Moulinec, H., Suquet, P., 1998. A numerical method for computing the overall response of nonlinear composites with complex microstructure. Comput. Methods Appl. Mech. Eng. 157 (1–2), 69–94.
- Murayama, Y., Hanada, S., 2002. High temperature strength, fracture toughness and oxidation resistance of Nb–Si–Al–Ti multiphase alloys. Sci. Technol. Adv. Mater. 3 (2), 145–156.
- Nakamura, T., Wang, T., Sampath, S., 2000. Determination of properties of graded materials by inverse analysis and instrumented indentation. Acta Mater. 48 (17), 4293–4306.
- Nebozhyn, M.V., Gilormini, P., Castañeda, P.P., 2001. Variational self-consistent estimates for cubic viscoplastic polycrystals: the effects of grain anisotropy and shape. J. Mech. Phys. Solid. 49 (2), 313–340.
- Nemat-Nasser, S., Hori, M., 2013. Micromechanics: Overall Properties of Heterogeneous Materials. Elsevier.
- Nix, W.D., Gao, H., 1998. Indentation size effects in crystalline materials: a law for strain gradient plasticity. J. Mech. Phys. Solid. 46 (3), 411–425.
- O'Neill, H., 1967. Hardness Measurement of Metals and Alloys. Chapman & Hall. Okamoto, A., 1989. Graphite formation in high-purity cold-rolled carbon steels. Metall. Mater. Trans. 20 (10), 1917–1925.
- Oliver, W.C., Pharr, G.M., 1992. An improved technique for determining hardness and elastic modulus using load and displacement sensing indentation experiments. J. Mater. Res. 7 (6), 1564–1583.
- Oliver, W.C., Pharr, G.M., 2004. Measurement of hardness and elastic modulus by instrumented indentation: advances in understanding and refinements to methodology. J. Mater. Res. 19 (1), 3–20.
- Otsu, N., 1979. A threshold selection method from gray-level histograms. IEEE transactions on systems, man, and cybernetics 9 (1), 62–66.
- Pan, Z., et al., 2018. Microstructure and mechanical properties of a cold-rolled ultrafinegrained dual-phase steel. Materials 11 (8), 1399.
- Pantazopoulos, G., et al., 2016. Analysis of the degradation process of structural steel component subjected to prolonged thermal exposure. Metallograph. Microstructuree. Analysis 5 (2), 149–156.

- Paredes-Orta, C.A., et al., 2019. Method for grain size determination in carbon steels based on the ultimate opening. Measurement 133, 193–207.
- Parvinian, S., et al., 2020. High-throughput exploration of the process space in 18% Ni (350) maraging steels via spherical indentation stress-strain protocols and Gaussian process models. Integrating Mater. Manufacturing Innovar. 9 (3), 199–212.
- Patel, D.K., Kalidindi, S.R., 2016. Correlation of spherical nanoindentation stress-strain curves to simple compression stress-strain curves for elastic-plastic isotropic materials using finite element models. Acta Mater. 112, 295–302.
- Pathak, S., Kalidindi, S.R., 2015. Spherical nanoindentation stress-strain curves. Mater. Sci. Eng. R Rep. 91, 1–36.
- Pathak, S., et al., 2008. Analyzing indentation stress–strain response of LaGaO 3 single crystals using spherical indenters. J. Eur. Ceram. Soc. 28 (11), 2213–2220.
- Pathak, S., Shaffer, J., Kalidindi, S.R., 2009a. Determination of an effective zero-point and extraction of indentation stress–strain curves without the continuous stiffness measurement signal. Scripta Mater. 60 (6), 439–442.
- Pathak, S., Stojakovic, D., Kalidindi, S.R., 2009b. Measurement of the local mechanical properties in polycrystalline samples using spherical nanoindentation and orientation imaging microscopy. Acta Mater. 57 (10), 3020–3028.
- Pathak, S., et al., 2012. Studying grain boundary regions in polycrystalline materials using spherical nano-indentation and orientation imaging microscopy. J. Mater. Sci. 47 (2), 815–823.
- Pathak, S., Kalidindi, S.R., Mara, N.A., 2016. Investigations of orientation and length scale effects on micromechanical responses in polycrystalline zirconium using spherical nanoindentation. Scripta Mater. 113, 241–245.
- Payton, E., Phillips, P., Mills, M., 2010. Semi-automated characterization of the  $\gamma'$  phase in Ni-based superalloys via high-resolution backscatter imaging. Mater. Sci. Eng A. 527 (10–11), 2684–2692.
- Peregrina-Barreto, H., et al., 2013. Automatic grain size determination in microstructures using image processing. Measurement 46 (1), 249–258.
- Perez, F., Granger, B.E., Hunter, J.D., 2011. Python: an ecosystem for scientific computing. Comput. Sci. Eng. 13 (2), 13–21.
- Pérez, I.Ü., et al., 2011. Graphitization in low alloy steel pressure vessels and piping. J. Fail. Anal. Prev. 11 (1), 3–9.
- Pharr, G.M., Herbert, E.G., Gao, Y., 2010. The indentation size effect: a critical examination of experimental observations and mechanistic interpretations. Annu. Rev. Mater. Res. 40, 271–292.
- Qian, L., et al., 2005. Comparison of nano-indentation hardness to microhardness. Surf. Coating. Technol. 195 (2–3), 264–271.
- Rodriguez, R., Gutierrez, I., 2003. Correlation between nanoindentation and tensile properties: influence of the indentation size effect. Mater. Sci. Eng A. 361 (1–2), 377–384.
- Santofimia, M., et al., 2008. Characterization of the microstructure obtained by the quenching and partitioning process in a low-carbon steel. Mater. Char. 59 (12), 1758–1764.
- Schemmann, L., et al., 2015. Alloying effects on microstructure formation of dual phase steels. Acta Mater. 95, 386–398.
- Segurado, J., Llorca, J., 2002. A numerical approximation to the elastic properties of sphere-reinforced composites. J. Mech. Phys. Solid. 50 (10), 2107–2121.
- Segurado, J., Llorca, J., 2013. Simulation of the deformation of polycrystalline nanostructured Ti by computational homogenization. Comput. Mater. Sci. 76, 3–11.
- Segurado, J., Gonzalez, C., Llorca, J., 2003. A numerical investigation of the effect of particle clustering on the mechanical properties of composites. Acta Mater. 51 (8), 2355–2369
- Smith, T., et al., 2018. A quantifiable and automated volume fraction characterization technique for secondary and tertiary  $\gamma'$  precipitates in Ni-based superalloys. Mater. Char. 140, 86–94.
- Soille, P., 2013. Morphological Image Analysis: Principles and Applications. Springer Science & Business Media.
- Stringfellow, R.G., Parks, D.M., 1991. A self-consistent model of isotropic viscoplastic behavior in multiphase materials. Int. J. Plast. 7 (6), 529–547.

- Suquet, P.M., 1985. Elements of homogenization for inelastic solid mechanics, homogenization techniques for composite media. Lect. Notes Phys. 272, 193.
- Swadener, J., George, E., Pharr, G., 2002. The correlation of the indentation size effect measured with indenters of various shapes. J. Mech. Phys. Solid. 50 (4), 681–694.
- Syn, C., Lesuer, D., Sherby, O., 1994. Influence of microstructure on tensile properties of spheroidized ultrahigh-carbon (1.8 Pct C steel. Metall. Mater. Trans. 25 (7), 1481–1493.
- Tabor, D., 1948. A simple theory of static and dynamic hardness. In: Proceedings of the Royal Society of London A: Mathematical, Physical and Engineering Sciences. The Royal Society.
- Tabor, D., 2000. The Hardness of Metals. Oxford university press.
- Tamura, T.Y., Ozawa, H., 1973. Proceedings of the Third International Conference on Strength of Metals and Alloys. Institute of Metal and Iron and Steel Institute, London.
- Tasan, C.C., et al., 2015. An overview of dual-phase steels: advances in microstructureoriented processing and micromechanically guided design. Annu. Rev. Mater. Res. 45, 391–431.
- Tirupataiah, Y., Sundararajan, G., 1991. On the constraint factor associated with the indentation of work-hardening materials with a spherical ball. Metall. Trans. A 22 (10), 2375–2384.
- Tomé, C.N., 1999. Self-consistent polycrystal models: a directional compliance criterion to describe grain interactions. Model. Simulat. Mater. Sci. Eng. 7 (5), 723.
- Torquato, S., 1991. Random Heterogeneous Media: Microstructure and Improved Bounds on Effective Properties.
- Torquato, S., 2002. Random Heterogeneous Materials: Microstructure and Macroscopic Properties, vol. 16. Springer.
- Torquato, S., 2013. Random Heterogeneous Materials: Microstructure and Macroscopic Properties, vol. 16. Springer Science & Business Media.
- Torquato, S., Stell, G., 1982. Microstructure of two-phase random media. I. The n-point probability functions. J. Chem. Phys. 77 (4), 2071–2077.
- Vachhani, S.J., Kalidindi, S.R., 2015. Grain-scale measurement of slip resistances in aluminum polycrystals using spherical nanoindentation. Acta Mater. 90, 27–36.
- Vachhani, S.J., Doherty, R.D., Kalidindi, S.R., 2016. Studies of grain boundary regions in deformed polycrystalline aluminum using spherical nanoindentation. Int. J. Plast. 81, 87–101.
- Walley, S.M., 2012. Historical origins of indentation hardness testing. Mater. Sci. Technol. 28 (9–10), 1028–1044.
- Weaver, J.S., Kalidindi, S.R., 2016. Mechanical characterization of Ti-6Al-4V titanium alloy at multiple length scales using spherical indentation stress-strain measurements. Mater. Des. 111, 463–472.
- Weaver, J.S., et al., 2016a. On capturing the grain-scale elastic and plastic anisotropy of alpha-Ti with spherical nanoindentation and electron back-scattered diffraction.

  Acta Mater. 117, 23–34.
- Weaver, J.S., et al., 2016b. High throughput exploration of process-property linkages in Al-6061 using instrumented spherical microindentation and microstructurally graded samples. Integrating Mater. Manufacturing Innovar. 5 (1), 1–20.
- Weaver, J., et al., 2017. Nanoindentation of Electropolished FeCrAl Alloy Welds. Los Alamos National Laboratory (LANL).
- Williamson, R., Rabin, B., Drake, J., 1993. Finite element analysis of thermal residual stresses at graded ceramic-metal interfaces. Part I. Model description and geometrical effects. J. Appl. Phys. 74 (2), 1310–1320.
- Wu, X., et al., 2015. Heterogeneous lamella structure unites ultrafine-grain strength with coarse-grain ductility. Proc. Natl. Acad. Sci. Unit. States Am. 112 (47), 14501–14505
- Zhang, P., Li, S., Zhang, Z., 2011. General relationship between strength and hardness. Mater. Sci. Eng A. 529, 62–73.
- Zhu, W., et al., 2019. A novel high-strength  $\beta$ -Ti alloy with hierarchical distribution of  $\alpha$ -phase: the superior combination of strength and ductility. Mater. Des. 168, 107640.